Chapter 1: Framing and Context

Technical Annex 1.A

This Annex provides technical details of the calculations behind the figures in the chapter, as well as some supporting figures provided for sensitivity analysis or to provide support to the main assessment.

Table of Content

Annex 1.A.1: supporting material for for Figure 1.1

Externally-forced warming is calculated for the Cowtan & Way (Cowtan and Way, 2014) dataset at every location and for each season as in Figure 1.3. The season with the greatest externally-forced warming at every location (averaged over the 2006-2015 period) is selected to give the colour of the dots at that grid box.

Technical Annex 1.A Figure 1 shows the season of maximum warming in each grid-box used in Figure 1.1, while Technical Annex 1.A Figure 2 shows the warming to 2006-2015 in the season that has warmed the least.
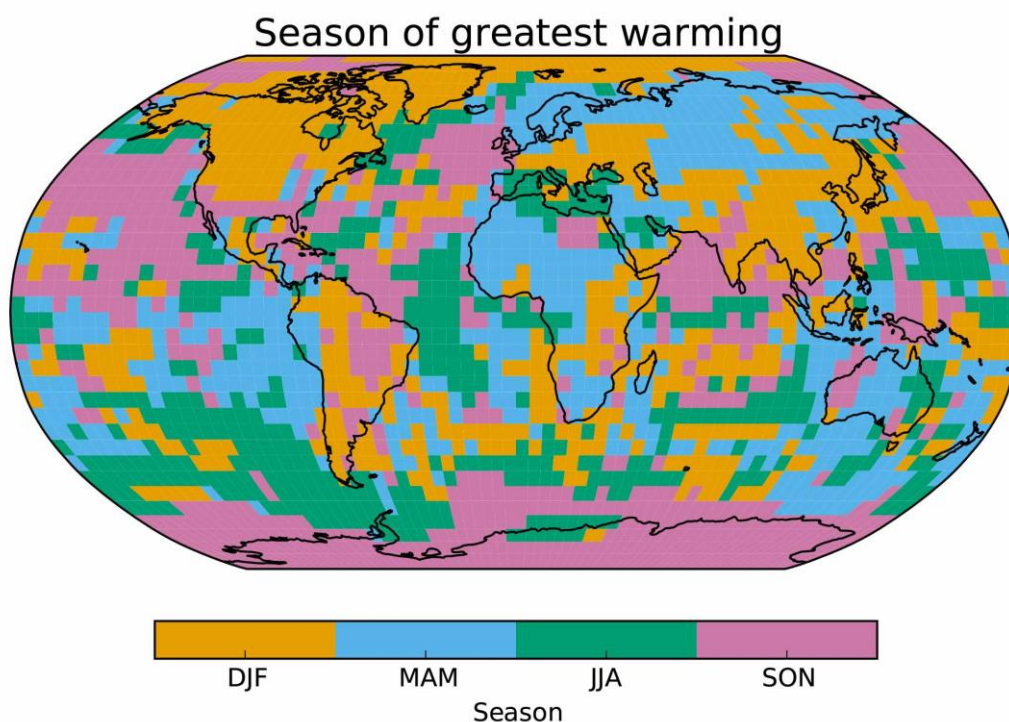

Technical Annex 1.A, Figure 1: Season of greatest human-induced warming over 2006-2015 relative to 1850-1900 for the data shown in Figure 1.1.
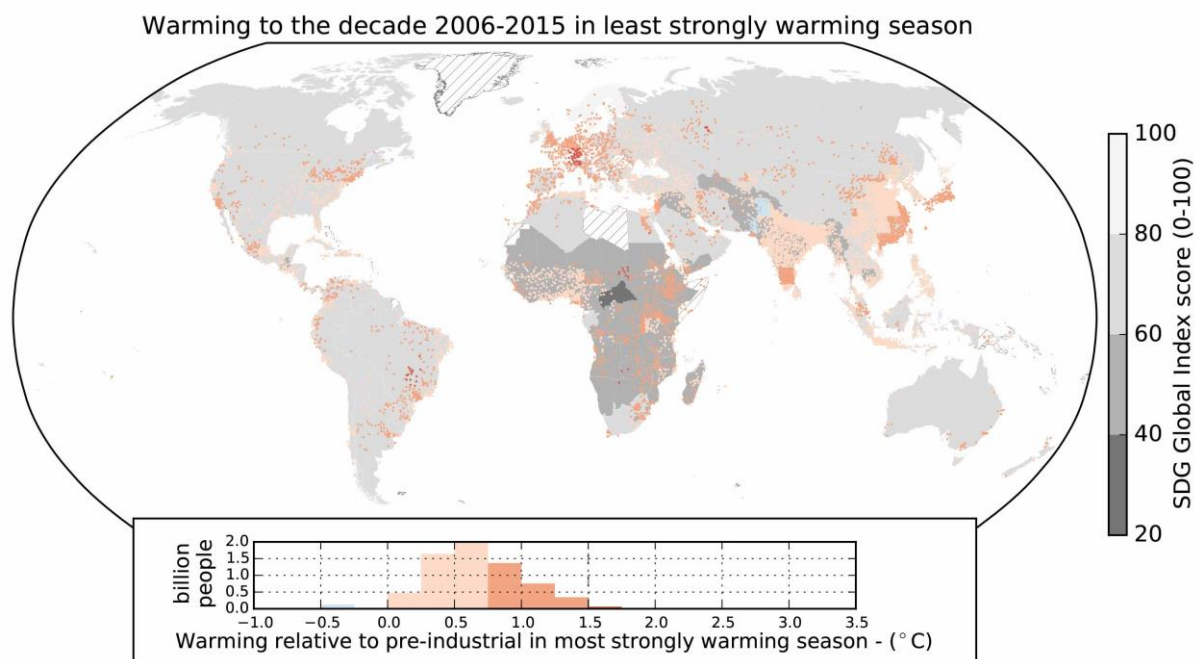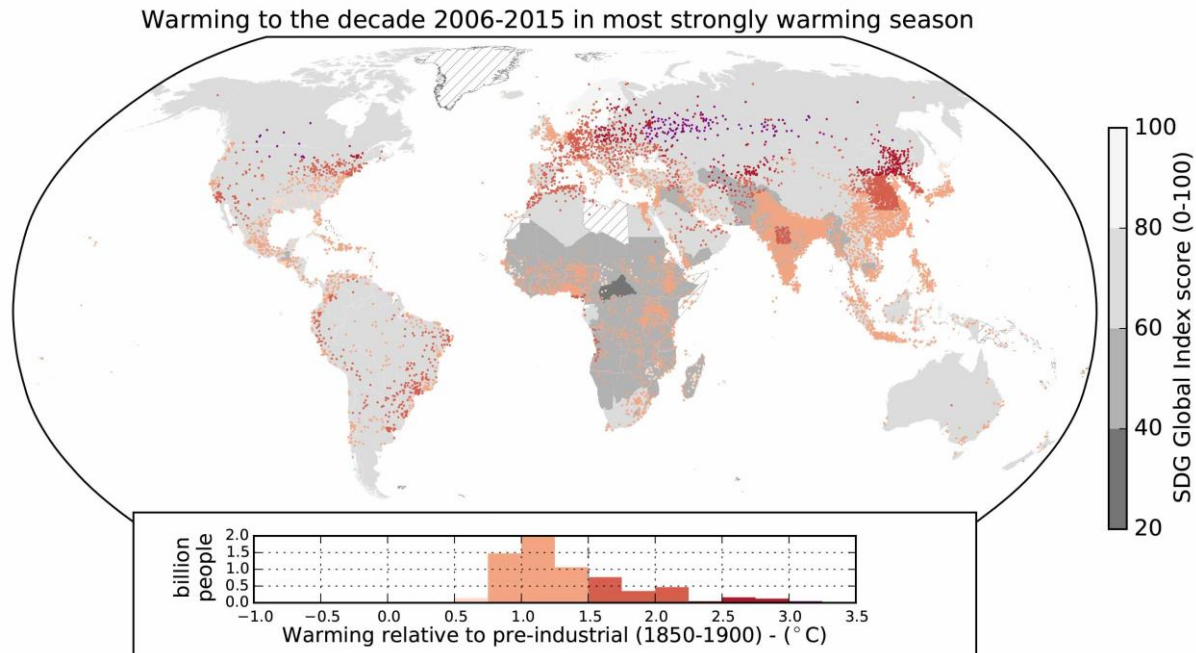
Technical Annex 1.A, Figure 2: As for Figure 1.1 but with scatter points coloured by warming in the season with least warming over the 2006-2015 period.

Population data is taken from Doxsey-Whitfield et al. (2015) for 2010. The number of scatter points shown in each 1°x1° grid box is directly proportional to the population count in the grid-box, with a maximum number of scatter points in a single grid-box associated with the maximum population count in the dataset. For grid-boxes with (non-zero) population counts that are below the population threshold consistent with just a single scatter point (approximately 650,000), the probability that a single scatter point is plotted reduces from unity towards zero with decreasing population in the grid-box to give an accurate visual impression of population distribution.

The SDG Global Index Score is a quantitative measure of progress towards the 17 sustainable development goals (Sachs et al., 2017). The goals cross-cut the three dimensions of sustainable development – environmental sustainability, economic growth, and social inclusion. It has a range of 0-100, 100 corresponding to all SDGs being met. Versions of Figure 1.1 using the HadCRUT4, NOAA and GISTEMP temperature datasets are shown in Technical Annex 1.A Figure 3-5 respectively.
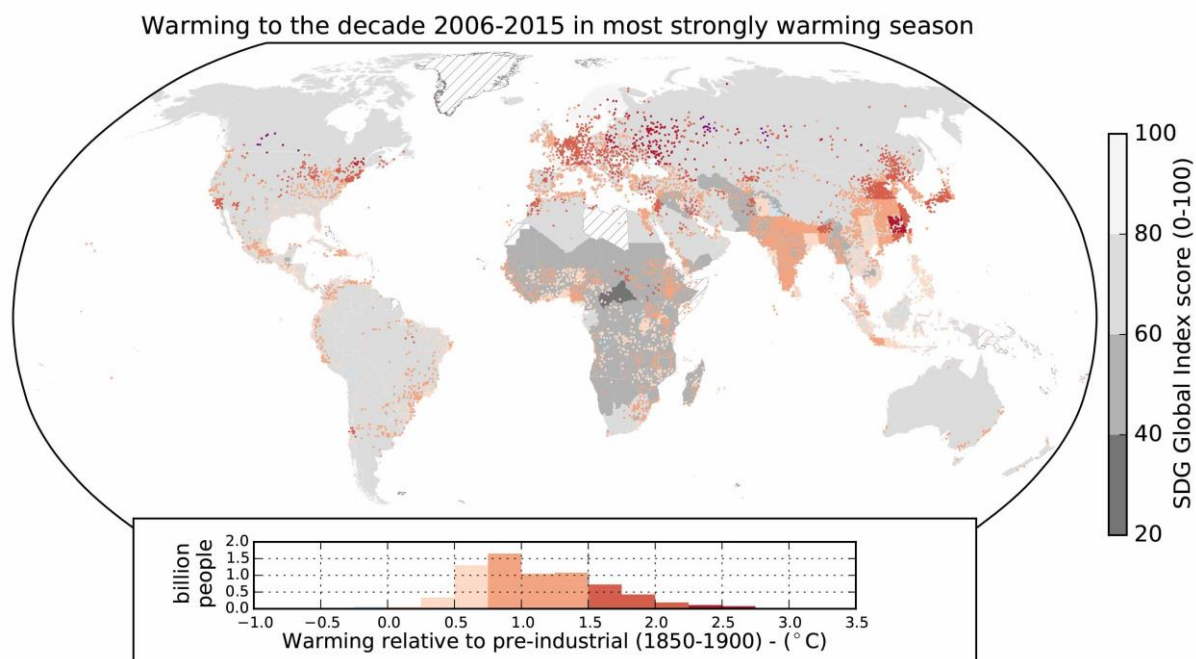
Technical Annex 1.A, Figure 3: As for Figure 1.1 but using the HadCRUT4 temperature dataset.

Technical Annex 1.A, Figure 4: As for Figure 1.1 but using the NOAA temperature dataset.
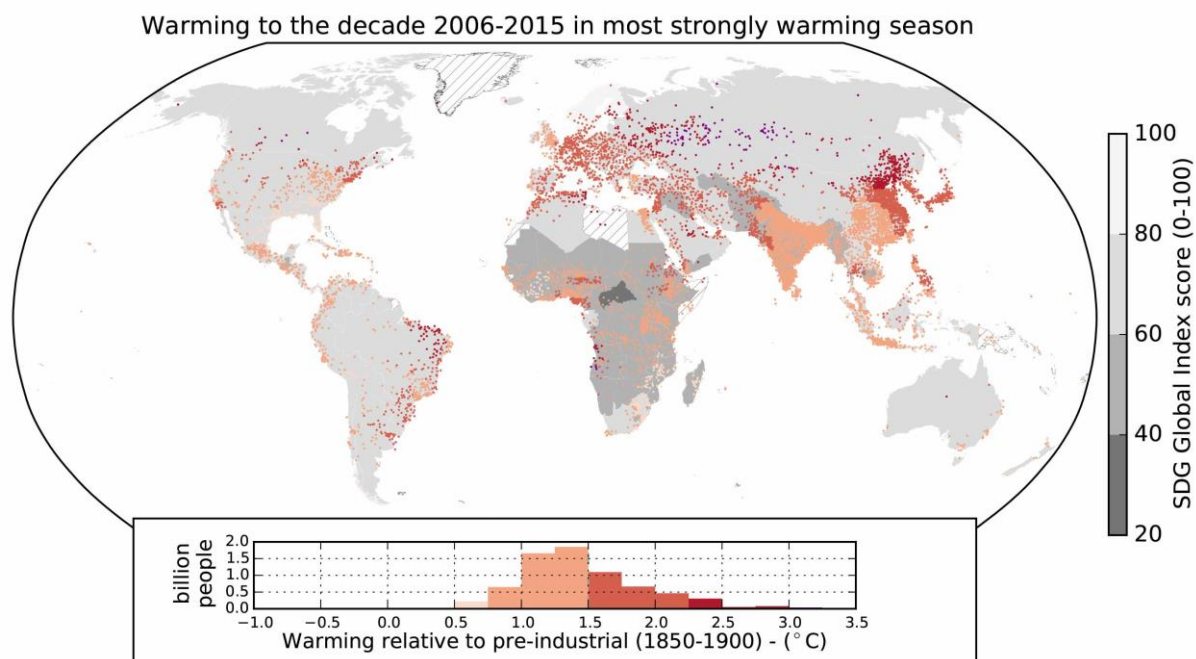
Technical Annex 1.A, Figure 5: As for Figure 1.1 but using the GISTEMP temperature dataset.

Annex 1.A.2: supporting material for Figure 1.2

Observational data used in Chapter figure 1.2 are taken from the Met Office Hadley Centre (http://www.metoffice.gov.uk/hadobs/hadcrut4/), National Oceanic and Atmospheric Administration (NOAA) (https://www.ncdc.noaa.gov/data-access/marineocean-data/noaa-global-surface-temperature-noaaglobaltemp), NASA's Goddard Institute for Space Studies (https://data.giss.nasa.gov/gistemp/) and the Cowtan & Way dataset (http://www-users.york.ac.uk/~kdc3/papers/coverage2013/series.html). The GISTEMP and NOAA observational products (which begin in 1880) are expressed relative to 1850-1900 by assigning these datasets the same anomaly as HadCRUT4 for the mean of the 1880-2017 period. All available data is used, through to the end of 2017, for all datasets. The grey "Observational range" shades between the minimum and maximum monthly-mean anomaly across these four temperature datasets for the month in question.

CMIP5 multi-model means, light blue dashed (full field surface air temperature) and solid (masked and blended as in Cowtan et al. (2015)) are expressed relative to a 1861-1880 base period and then expressed relative to the 1850-1900 reference period using the anomaly between the periods in the HadCRUT4 product (0.02°C). Model data are taken from Richardson et al. (2018). Only RCP8.5 r1i1p1 ensemble members are used with only one ensemble member per model for calculating the mean lines in this figure.

The pink "Holocene" shading is derived from the "Standard5x5Grid" reconstruction of Marcott et al. (2013) (expressed relative to 1850-1900 using the HadCRUT4 anomaly between this reference period and the 1961-90 base period of the data). The vertical extent of the solid shading is determined by the maximum and minimum temperature anomalies in the dataset in the period before 1850. Marcott et al. (2013) report data with a periodicity of 20 years, so the variability shown by the solid pink shading is not directly comparable to the higher frequency variability seen in the observational products which are reported every month), but this Holocene range can be compared to the emerging signal of

human-induced warming. Above and below the maximum and minimum temperature anomalies from Marcott et al. (2013) the pink shading fades out to after a magnitude of warming that is equal to the standard deviation of monthly temperature anomalies in the HadCRUT4 dataset over the pre-industrial reference period of 1850-1900, and as such this faded shading does not bound all monthly anomalies in the pre-industrial reference period.

Near term predictions from IPCC-AR5 (Kirtman et al., 2013), for the period 2016-2035 were estimated to be *likely* (>66% probability) between 0.3°C and 0.7°C above the 1986-2005 average, assuming no climatically significant future volcanic eruptions. These are expressed relative to pre-industrial using the updated 0.63°C warming to the 1986-2005 period (Section 1.2.1).

Human-induced temperature change (thick yellow line) and total (human+natural) externally-forced temperature change (thick orange line) are estimated using the method of Haustein et al. (2017) applied to the 4-dataset mean. Best-estimate historical radiative forcings, extended until the end of 2016, are taken from Myhre et al. (2013), incorporating the significant revision to the methane forcing proposed by Etminan et al. (2016). The 2-box thermal impulse-response model used in Myhre et al. (2013), with modified thermal response time-scales to match the multi-model mean from Geoffroy et al. (2013), is used to derive the shape to the global mean temperature response timeseries to total anthropogenic and natural (combined volcanic and solar) forcing. Both of these timeseries are expressed as anomalies relative to their simulated 1850-1900 averages and then used as independent regressors in a multi-variate linear regression to derive scaling factors on the two timeseries that minimise the residual between the combined forced response and the multi-dataset observational mean. The transparent shading around the thick yellow line indicates the *likely* range in attributed human-induced warming conservatively assessed at ±20%. Note that the corresponding *likely* range of ±0.1°C uncertainty in the 0.7°C best-estimate anthropogenic warming trend over the 1951-2010 period assessed in Bindoff et al. (2013) corresponds to a smaller fractional uncertainty (±14%): the broader range reflects greater uncertainty in early-century warming.

The vertical extent of the 1986-2005 cross denotes the 5-95% observational uncertainty range of ±0.06°C (see Table 1.1) while that of the 2006-2015 cross denotes the assessed *likely* uncertainty range of ±0.12°C (Section 1.2.1).

To provide a methodologically independent check on the attribution of human-induced warming since the 19th century (quantitative attribution results quoted in AR5 being primarily focussed on the period 1951-2010), Technical Annex 1.A Figure 6 shows a recalculation of the results of Ribes and Terray (2013), figure 1, applied to the CMIP5 multi-model mean response. Details of the calculation are provided in the original paper. In order to quantify the level of human-induced warming since the late 19th century, observations of GMST are regressed onto the model responses to either natural-only (NAT) or anthropogenic-only (ANT) forcings, consistent with many attribution studies assessed in AR5. Prior to this analysis, model outputs are pre-processed in order to ensure consistency with observations: spatial resolution is lowered to 5°, the spatio-temporal observational mask is applied, and all missing data are set to 0. Global and decadal averages of near-surface temperature are calculated over the 1901-2010 period (11 decades), and translated into anomalies by subtracting the mean over the entire period (1901-2010). Multi-model mean response patterns are calculated over a subset of 7 CMIP5 models providing at least 4 historical simulations and 3 historical NAT-only simulations, all covering the 1901-2010 period. The regression analysis indicates how these multi-model mean responses have to be rescaled in order to best fit observations, accounting for internal variability in both observations and model responses, but neglecting observational uncertainty. Almost no rescaling is needed for ANT (regression coefficient: 1.05 ±0.18), while the NAT simulated response is revised downward (regression coefficient: 0.28±0.49). The resulting estimate of the total externally forced response is very close to observations (Figure 6). The ANT regression coefficient can then be used to assess the human-induced warming over a longer period. Estimated in this way, the human-induced linear warming trend 1880-2012 is found to be 0.86°C±0.14°C.
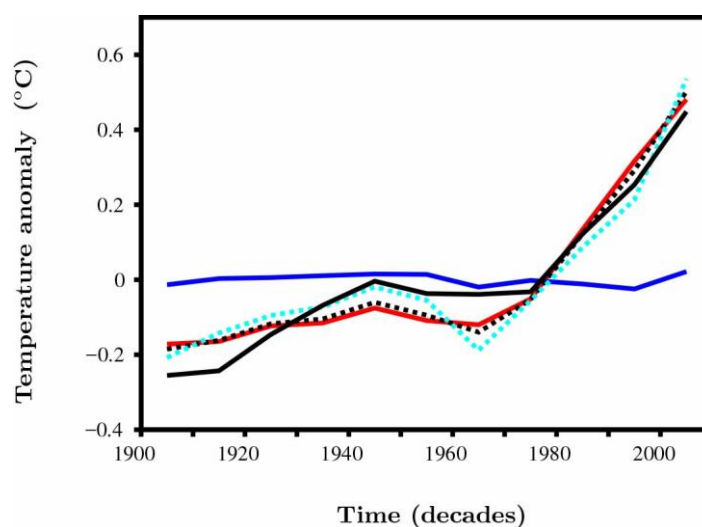
Technical Annex 1.A, Figure 6: Contributions of natural (NAT) and anthropogenic (ANT) forcings to changes in GMST over the period 1901-2010. Decadal time-series of GMST in HadCRUT4 observations (solid black), from multi-model mean response without any rescaling (dotted cyan), and as reconstructed by the linear regression (dotted black). The estimated contributions of NAT forcings only (solid blue) and anthropogenic forcing only (solid red) correspond to the CMIP5 multi-model mean response to these forcings, after rescaling. All temperatures are anomalies with respect to the 1901-2010 average, after pre-processing (missing data treated as 0). Vertices are plotted at the mid-point of the corresponding decade.

To quantify the potential impact of natural (externally-forced or internally-generated) variability on decadal-mean temperatures in 2006-2015, Technical Annex1.A Figure 7 shows an estimate of the observed warming rate, corrected for the effects of natural variability according to the method of Foster and Rahmstorf, (2011) applied to the average of the four observational datasets used in this report, updated to the end of 2017. The grey line shows the raw monthly GMST observations (with shading showing inter-dataset range), while the green shows the sum of the linear trend plus estimated known sources of variability, such as El Niño events or volcanic eruptions, estimated using an empirical regression model. The orange line shows the linear trend, after correcting for the impact of these known sources of variability, of 0.18°C per decade, while the two black lines show the recent reference periods used in this report. For comparison, the AR5 near-term predicted warming rate of 0.3-0.7°C over 30 years (Kirtman et al, 2013) is shown as the pale blue plume.

The blue line in the lower panel shows residual fluctuations that cannot be attributed to known sources or modes of variability, reflecting internally-generated chaotic weather variability (the difference between grey and green lines in the top panel). The green line is not persistently below the yellow line, nor is the blue line persistently negative, over the period 2006-2015. There is a downward excursion in the residual "unexplained" variability around 2012-13, and a strong ENSO cool phase event in 2011, but even together these depress the decadal average by only a couple of hundredths of a degree.
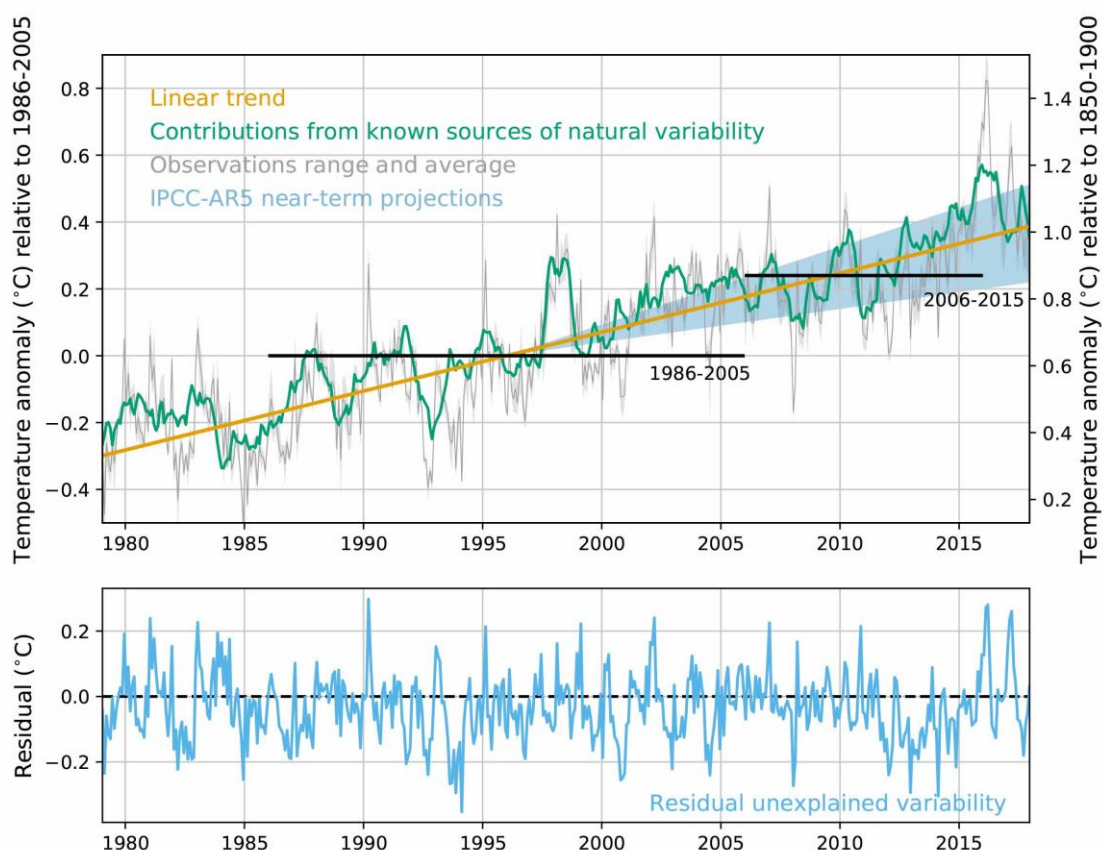
Technical Annex 1.A, Figure 7: Warming and warming rate 1979-2017. The solid grey line shows the average of the four observational datasets used in this assessment report with the observational range shown by grey shading. The yellow line shows the linear trend through the observational data, corrected for the effects of known sources of natural variability (green line). The blue shading indicates that warming rates compatible with the IPCC-AR5 near-term projections. The lower panel shows the residual unexplained variability (difference between grey and green lines in upper panel) after accounting for known sources, including ENSO, solar variability and volcanic activity.


Annex 1.A.3: supporting material for Figure 1.3

Regional warming shown in Figure 1.3 is derived using a similar method to the calculation of externally-forced warming in Figure 1.2. At every grid box location in the native Cowtan & Way resolution, the timeseries of local temperature anomalies in the Cowtan & Way dataset are regressed onto the associated externally-forced warming timeseries, calculated as in Figure 1.1 using all available historical monthly-mean anomalies. The best-fit relationship between these two quantities is then used to estimate the forced warming relative to 1850-1900 at this location. The maps in Figure 1.3 show the average of these estimated local forced warming timeseries over the 2006-2015 period. Trends are only plotted only where over 50% of the entire observational record at this location is available.

Supplementary maps are included below for the NOAA, GISTEMP and HadCRUT4 observational data. The regression of local temperature anomalies onto the global mean externally-forced warming, allows warming to be expressed relative to 1850-1900 despite many local series in these datasets

beginning after 1900, but clearly these inferred century-time-scale warming levels are subject to a lower confidence level than the corresponding global values.
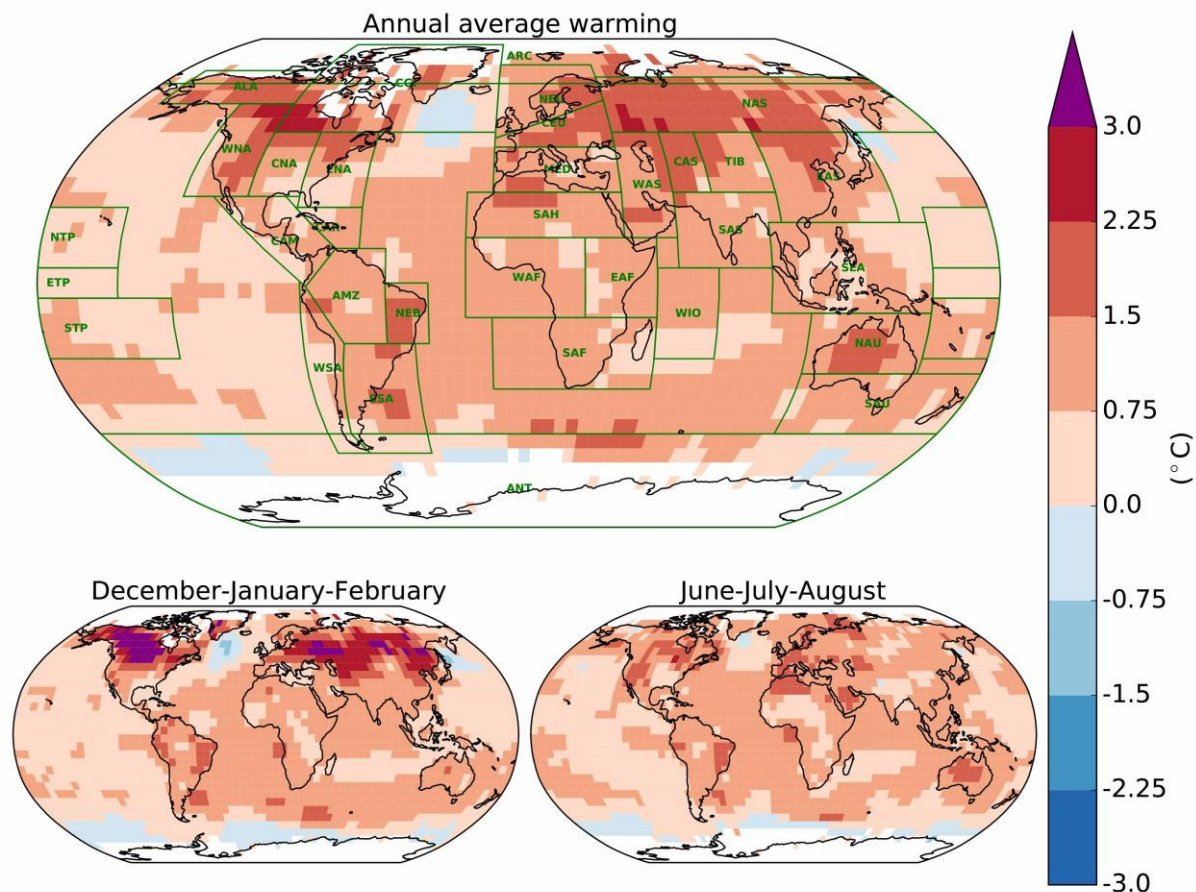
Technical Annex 1.A Figure 8: Externally-forced warming for the average of 2006-2015 relative to 1850-1900 calculated for the NOAA observational dataset as for Figure 1.3.

Regional warming in the decade 2006-2015 relative to preindustrial
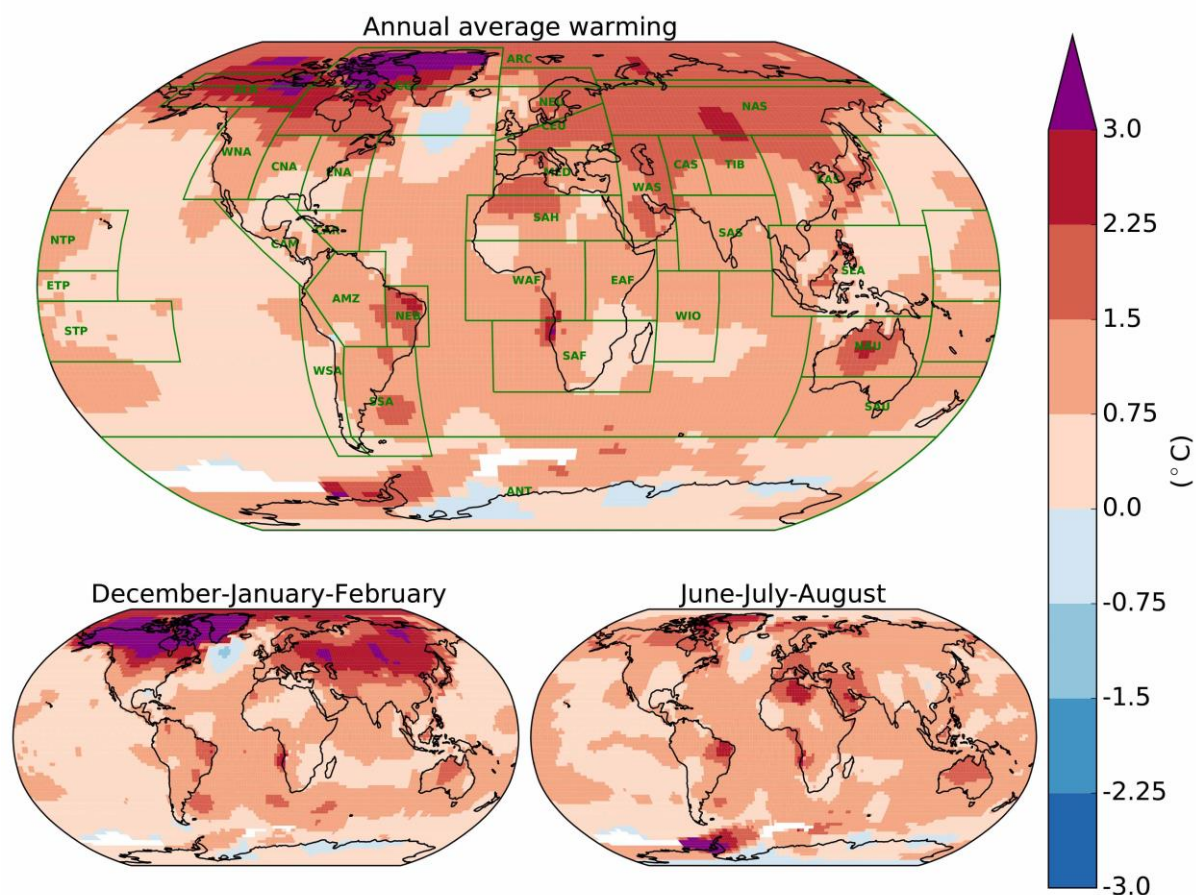
Technical Annex 1.A, Figure 9: Externally-forced warming for the average of 2006-2015 relative to 1850-1900 calculated for the GISTEMP observational dataset as for Figure 1.3.

Regional warming in the decade 2006-2015 relative to preindustrial

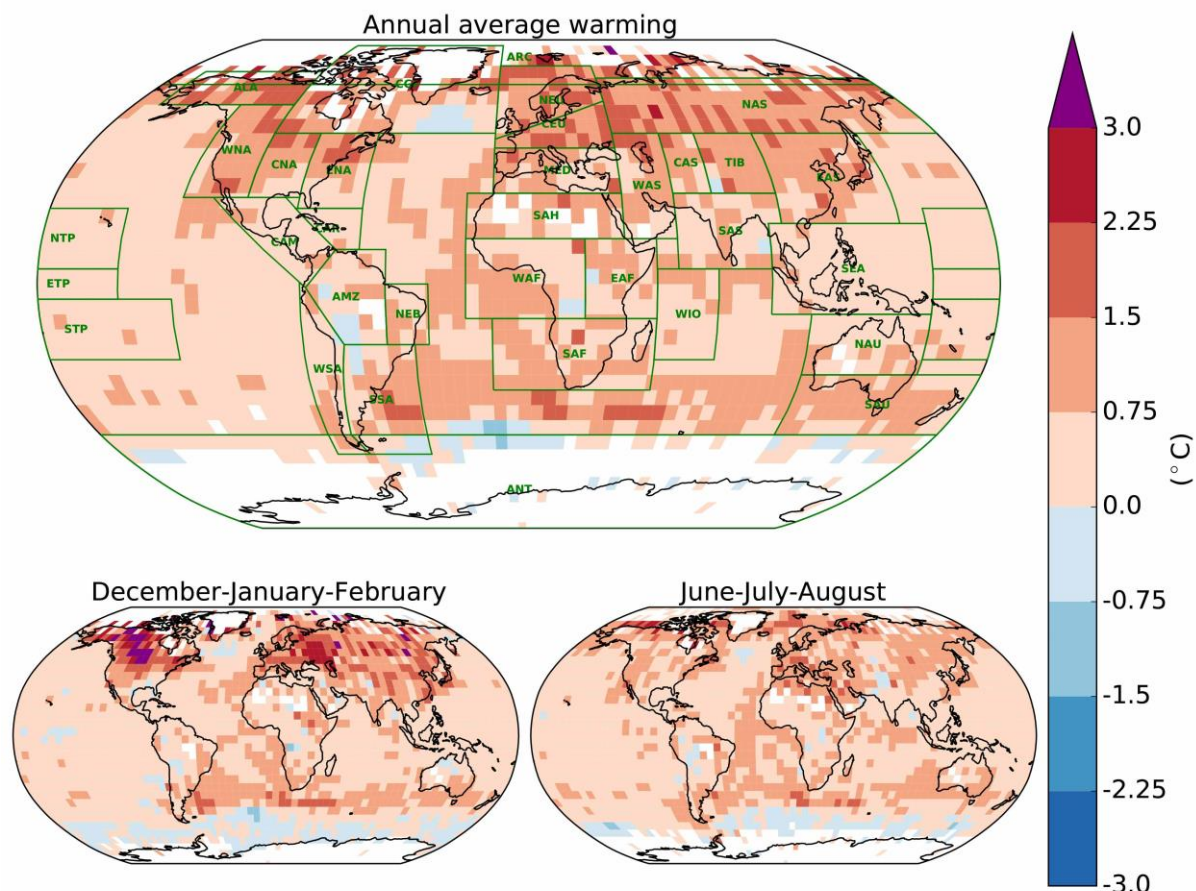**Technical Annex 1.A, Figure 10:** Externally-forced warming for the average of 2006-2015 relative to 1850-1900 calculated for the HadCRUT4 observational dataset as for Figure 1.3.

Annex 1.A.4: supporting material for Figure 1.4

Idealised temperature pathways computed by specifying the level of human-induced warming in 2017, $T_{2017} = 1°C$, with temperatures from 1850 to 2017 approximated by an exponential rise, with the exponential rate constant, γ, set to give a rate of human-induced warming in 2017 of 0.2°C/decade. Temperatures from 2018-2100 are determined by fitting a smooth 4th-order polynomial through specified warming at particular times after 2017.

Radiative forcing F that would give the temperature profiles is computed using a 2-time-constant climate response function (Myhre et al., 2013b), with Equilibrium Climate Sensitivity (ECS) of 2.7°C and Transient Climate Response (TCR) of 1.6°C and other parameters as given in Millar et al. (2017). Equivalent CO_2 concentrations given by $C = 278 \times \exp(F/5.4)$ ppm.

Cumulative CO_2-forcing-equivalent emissions (Jenkins et al, 2018), or the CO_2 emission pathways that would give the CO_2 concentration pathways compatible with the temperature scenario is computed using an invertible simple carbon cycle model (Myhre et al., 2013b), modified to account for changing CO_2 airborne fraction over the historical period (Millar et al., 2017). These are proportional to CO_2 emissions under the assumption of a constant fractional contribution of non-CO_2

forcers to warming. Indicative cumulative impact variable (e.g. sea level rise) is computed from temperature pathways shown in using semi-empirical model of Kopp et al. (2016).

Annex 1.A.5: supporting material for Figure 1.5

All scenarios in Figure 1.5 start with a 1000 member ensemble of the FAIR model (Smith et al., 2018) driven with emissions from the RCP historical dataset from 1765 to 2000 (Meinshausen et al., 2011), SSP2 from 2005 to 2020 (Fricko et al., 2017), and a linear interpolation between the two inventories for 2000 to 2005. Equilibrium climate sensitivity (ECS) and transient climate response (TCR) parameters are drawn from a joint lognormal distribution informed by CMIP5 models. Uncertainties in present-day non-CO_2 ERF are drawn from the distributions in Myhre et al. (2013) and uncertainties in the carbon cycle response are given a 5 to 95% range of 13% around the best estimate (Millar et al., 2017). All uncertainties except TCR and ECS are assumed to be uncorrelated with each other.

FAIR derives an effective radiative forcing (ERF) time series from emissions, from which temperature change calculated. Greenhouse gas concentrations are first calculated, from which the radiative forcing relationships from Myhre et al. (1998) are used to determine ERF. An increase of ERF of 25% for methane forcing is applied which approximates the updated relationship from Etminan et al. (2016). The Myhre et al. (1998) relationships with a scaling for methane rather than the newer Etminan et al. (2016) relationships are used because the former does not assume any band overlap between CO_2 and N_2O, and isolating CO_2 forcing from N_2O forcing is problematic for certain commitments where CO_2 emissions are set to zero and N_2O forcing is held constant.

Aerosol forcing is based on the Aerocom radiative efficiencies (Myhre et al., 2013a) for ERFari (ERF from aerosol-radiation interactions) and a logarithmic dependence on emissions of black carbon, organic carbon and sulfate for ERFaci (ERF from aerosol-cloud interactions) based on the model of Ghan et al., (2013). Tropospheric ozone forcing is based on Stevenson et al., (2013). Other minor categories of anthropogenic forcing are derived from simple relationships that approximate the evolution of ERF in Annex II of Working Group I of AR5 (Prather et al., 2013) as described in Smith et al., (2018). For forcing categories other than methane (for which a significant revision to be best estimate ERF has occurred since AR5), a time-varying scaling factor is implemented over the historical period, so that for a best estimate forcing, the AR5 ERF time series is replicated. This historical scaling decays linearly between 2000 and 2011 so that in 2011 onwards the FAIR ERF estimate is used for projections. For the 2000-2011 period the impact of the historical scaling is small, because FAIR emissions-forcing relationships are mostly derived from IPCC AR5 best estimates in 2005 or 2011 (Smith et al., 2018).

Two ensembles are produced: a historical (1765 to 2014) ensemble containing all (anthropogenic plus natural) forcing, and a historical+future (1765 to 2100) ensemble containing only anthropogenic forcing for each commitment scenario. In the ensemble where natural forcing is included, solar forcing for the historical period is calculated by using total solar irradiance from the SOLARIS HEPPA v3.2 dataset (Matthes et al., 2017) for 1850-2014 and from Myhre et al. (2013) for 1765-1850: the 1850-1873 mean is subtracted from the time series which is then multiplied by 0.25 (annual illumination factor) times 0.7 (planetary co-albedo) to generate the effective radiative forcing (ERF) timeseries. Volcanic forcing is taken by using stratospheric aerosol optical depths from the CMIP6 historical Easy Volcanic Aerosol dataset (Toohey et al., 2016) prepared for the HadGEM3 CMIP6 historical integrations for 1850-2014. The integrated stratospheric aerosol optical depth at 550 nm (tau) is calculated and converted to ERF by the relationship $ERF = -18 \cdot tau$, based on time slice experiments in the HadGEM3 general circulation model, which agrees well with earlier HadGEM2 and HadCM3 versions of the UK Met Office Hadley Centre model (Gregory et al., 2016). The 1850-2014 mean volcanic ERF of -0.107 is subtracted as an offset to define the mean historical volcanic

ERF as zero. Owing to rapid adjustments to stratospheric aerosol forcing, which are included in the definition of ERF, this less negative value of -18*tau is adopted for volcanic ERF than the RF = -25*tau used in AR5.

The historical all-forcing scenario is then used to constrain parameter sets that satisfy the historical observed temperature trend of $0.90 \pm 0.19°C$ (mean and 5 to 95% range) over the 1880 to 2014 period, using the mean of the HadCRUT4, GISTEMP and NOAA datasets. The trend was derived using an inflation factor for autocorrelation of residuals, and is the same method used to derive linear temperature trends in AR5 (Hartmann et al., 2013). The uncertainty bounds used here are wider than, but consistent with, the 1-sigma range of $\pm0.12°C$ assessed for the temperature change in 2006-2015 relative to 1850-1900. The parameter sets that satisfy the historical temperature constraint in the historical ensemble (323 out of 1000) are then selected for the anthropogenic-only ensembles that include commitments.

Each commitment scenario is driven with the following assumptions:

1.   Zero CO_2 emissions, constant non-CO2 forcing (blue): FAIR spun up with anthropogenic forcing to 2020. Total non-CO_2 forcing in 2020 is used as the input to the 2021-2100 period with all CO_2 fossil and land use emissions abruptly set to zero.

2.   Phase out of CO_2 emissions with 1.5°C commitment (blue dotted): FAIR spun up with anthropogenic forcing to 2020. Total non-CO_2 forcing in 2020 is used as the input to the 2021-2100 periof. Fossil and land-use CO_2 emissions are ramped down to zero at a linear rate over 50 years from 2021 to 2070, consistent with a 1.5°C temperature rise since pre-industrial at the point of zero CO_2 emissions in 2070.

3.   Linear continuation of 2010-2020 temperature trend (blue dashed, in bottom panel only).

4.   Zero GHG emissions, constant aerosol forcing (pink): FAIR spun up with anthropogenic forcing to 2020. All GHG emissions set abruptly to zero in 2021, with aerosol emissions held fixed at their 2020 levels.

5.   Zero CO_2 and aerosol emissions, constant non-CO_2 GHG forcing (teal): FAIR spun up with anthropogenic forcing to 2020. Total non-CO_2 GHG forcing, which also includes the proportion of tropospheric ozone forcing attributable to methane emissions, in 2020 is used as the input to the 2021-2100 period. Fossil and land-use CO_2 and aerosol emissions abruptly set to zero in 2021.

6.   Zero emissions (yellow): FAIR spun up with anthropogenic forcing to 2020. All emissions set abruptly to zero in 2021.

Annex 1.A.6: supporting material for FAQ 1.2 Figure 1 and Figure SPM1

This section provides supporting material for the figure in FAQ 1.2 and the figure SPM1 in the Summary for Policymakers. Figure 11, top panel, shows time-series of annual CO_2 emissions from the Global Carbon Project (Le Quéré et al, 2018) (black line and grey band, with the width of the band indicating the *likely* range, or one-standard-error, uncertainty in annual emissions), extrapolated to 2020 and then declining in a straight line to reach net zero in either 2055 (green line) or 2040 (brown line).
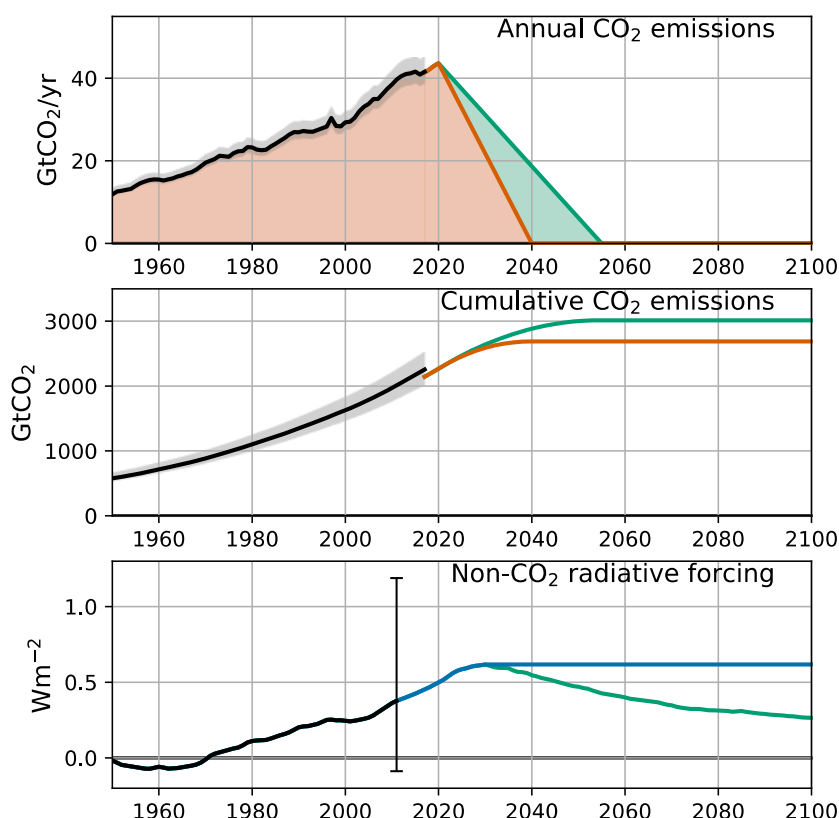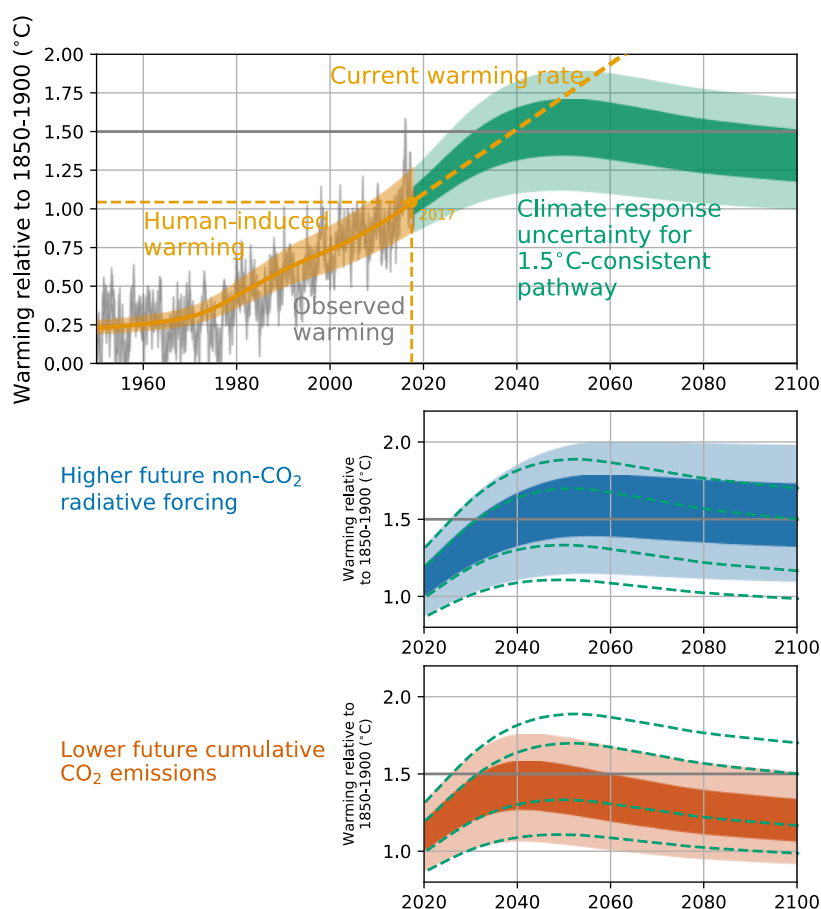
Technical Annex 1.A, Figure 11: Time-series of (top) annual CO_2 emissions, (middle) cumulative CO_2 emissions, and (bottom) non-CO_2 radiative forcing corresponding to observation-based estimates over the historical period and idealised 1.5°C-consistent pathways.

The middle panel in figure 11 shows cumulative (time-integrated) CO_2 emissions, or the areas highlighted as brown+green or brown, respectively, in the top panel. Brown and green lines show cumulative emissions diagnosed from a simple climate-carbon-cycle model (Millar et al, 2017), with historical airborne fraction scaled to reproduce median estimated annual emissions in 2017. Note this does not precisely reproduce median estimated cumulative emissions in 2017, but is well within the range of uncertainty.

The bottom panel in figure 11 shows median non-CO2 effective radiative forcing (ERF) estimates used to drive the model over the historical period, extending forcing components using the RCP8.5 scenario (http://www.pik-potsdam.de/~mmalte/rcps/) between 2011 and 2020, with scaling applied to each full forcing component time-series to match the corresponding AR5 ERF component in 2011. The vertical bar in 2011 shows a simple indication of the *likely* range of non-CO_2 forcing in 2011 obtained simply by subtracting the best-estimate CO_2 forcing from the total anthropogenic forcing uncertainty, assuming the latter is normally distributed: AR5 did not give a full assessment of the distribution of non-CO_2 radiative forcing. It demonstrates there is considerable uncertainty in this quantity, which translates into uncertainty in climate system properties inferred from these data, but has a much smaller impact on estimates of human-induced warming to date, because this is also constrained by temperature observations. The green line shows non-CO_2 forcing in an indicative 1.5°C-consistent pathway consistent with those assessed by Chapter 2, while the blue line shows an idealised case in which non-CO_2 forcing remains constant after 2030.

For all percentiles of the climate response distribution, non-CO_2 forcing timeseries for these idealised scenarios are scaled to allow the corresponding percentiles of the assessed *likely* range of human-induced warming in 2017 to be achieved, assuming the latter is normally distributed. All non-CO_2 forcing components other than aerosols are scaled following their corresponding ranges of uncertainty of values in 2011 given in AR5, with low values of 2011 ERF corresponding to high values of TCR and *vice versa*. This accounts for the anti-correlation between estimated values of the TCR and estimates of current anthropogenic forcing. Then aerosol ERF (the most uncertain component) is scaled to reproduce the correct percentile of human-induced warming in 2011. Values of TCR, ECS and 2011 forcing components are given in Technical Annex 1.A Table 1.

Figure 12 shows timeseries of observed and human-induced warming to 2017 and responses to these idealised future emissions scenarios. Observed and human-induced warming estimates are reproduced exactly as in Figure 1.2, with the orange shaded band showing the assessed uncertainty range of ±20%. The dashed line shows a simple linear extrapolation of the current rate of warming, as calculated over the past 5 years. Responses to idealized future CO_2 emissions and non-CO_2 forcing trajectories are simulated with the FAIR simple climate-carbon-cycle model (Millar et al, 2017b). The four values of the Transient Climate Response (TCR) shown (giving the borders of the green, blue and orange shaded regions) correspond to the 17th, 33rd, 67th and 83rd percentiles of a normal distribution compatible with the *likely* range of TCR as assessed by AR5, combined with the same percentiles of a log-normal distribution for the Equilibrium Climate Sensitivity (ECS) similarly anchored to the AR5 *likely* range for this quantity. Other thermal climate response parameters (short and long adjustment time-scales) are set to match those given in Myhre et al (2013) as used in Millar et al (2017a).

Technical Annex 1.A, Figure 12: Time-series of observed and human-induced warming to 2017 and responses to idealised 1.5°C-consistent pathways of CO_2 and non-CO_2 forcing shown in figure 11.

All 1.5°C-consistent scenarios that are also consistent with current emissions and radiative forcing trends show increasing non-CO_2 radiative forcing over the coming decade, as emissions of cooling aerosol precursors are reduced, but there is greater variation between scenarios in non-CO_2 radiative forcing after 2030. The middle panel in figure 12 shows the impact of varying future non-CO_2 radiative forcing (green and blue lines in figure 11, bottom panel), while the green dashed lines show the original percentiles from the top panel. Failure to reduce non-CO_2 forcing after 2030 means that a scenario that would give temperatures *likely* below 1.5°C in 2100 instead give only temperatures *as likely as not* below 1.5°C by 2100. If non-CO_2 forcing were allowed to increase further (as it does in some scenarios due primarily to methane emissions), it would increase 2100 temperatures further.

The bottom panel of figure 12 shows the impact of reducing cumulative CO_2 emissions up to the time they reach net zero by bringing forward the date of net-zero emissions from 2055 to 2040. This reduces future warming, with the impact emerging after 2030, such that the entire *likely* range of future warming is now (on this estimate of the climate response distribution) below 1.5°C in 2100. These changes demonstrate how future warming is determined by cumulative CO_2 emissions up to the time of net-zero and non-CO_2 forcing in the decades immediately prior to that time.

Technical Annex 1.A, Table 1: Climate system properties in the versions of the FAIR model used in figures 12 and 13 of this Technical Annex as well as the FAQ 1.2 figure and figure SPM1. TCR, ECS and total anthropogenic forcing, F_{ant}, in 2011 are set consistent with corresponding distributions in AR5, TCRE is diagnosed from the model while aerosol forcing F_{aer} is adjusted to reproduce the corresponding percentile of human-induced warming in 2017.

Percentile	TCR (°C)	ECS (°C)	TCRE (°C/TtC)	F_{aer} in 2011 (W/m^2)	F_{ant} in 2011 (W/m^2)
17%	1.0	1.5	0.9	-0.67	3.02
33%	1.4	2.0	1.3	-0.95	2.46
50%	1.75	2.6	1.5	-0.99	2.20
67%	2.1	3.3	1.75	-0.95	2.01
83%	2.5	4.5	2.2	-0.84	1.84

Carbon budget calculations in Chapter 2 are based on temperatures relative to 2006-2015, offset by a constant 0.87°C representing the best-estimate observed warming from pre-industrial to that decade. This has little effect on median estimates of future warming, because the median estimated human-induced warming to the decade 2006-2015 was close to the observed warming, but it does affect uncertainties: the uncertainty in 2030 warming relative to 2006-2015 is lower than the uncertainty in 2030 warming relative to pre-industrial because of the additional information provided by the current climate state and trajectory. This additional information is particularly important for the response to rapid mitigation scenarios in which peak warming occurs a small number of decades into the future (Millar et al, 2017a; Leach et al, 2018), highlighting the particular importance of a "seamless" approach to seasonal-to-decadal forecasting (Palmer et al, 2008; Boer et al, 2016) in the context of 1.5°C. The impact of this additional information is illustrated in figure 13, which is constructed identically to figure 12 but shows all time-series expressed as anomalies relative to 2006-2015 rather than 1850-1900. The thick grey line at 0.63°C shows 1.5°C relative to pre-industrial expressed relative to this more recent decade. The central estimate is unaffected, as is the estimate of the time at which temperatures reach 1.5°C if the current rate of warming continues, but uncertainties are reduced. For example, the idealised pathway with CO_2 emissions reaching zero in 2040 is *likely* to limit warming to less than 0.63°C above 2006-2015, even though it just overshoots 1.5°C relative to 1850-1900.
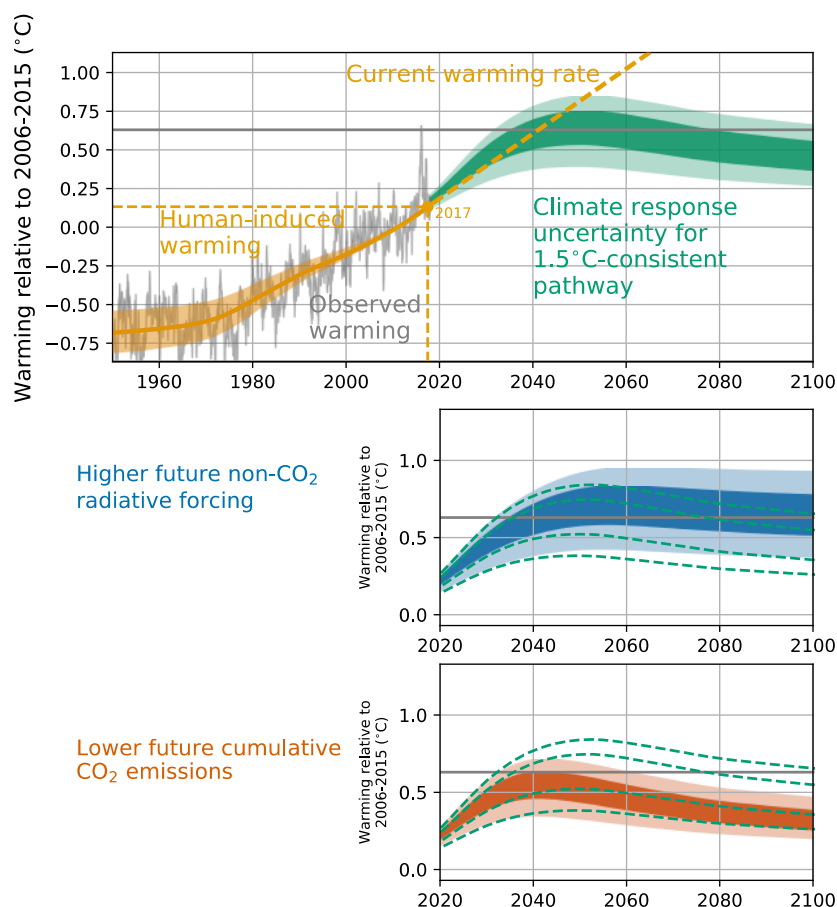
Technical Annex 1.A, Figure 13: As figure 12, but showing time-series of observed and human-induced warming to 2017 and responses to idealised 1.5°C-consistent pathways relative to 2006-2015. Level of warming corresponding to 1.5°C relative to pre-industrial given central estimate of observed warming of 0.87°C from 1850-1900 to 2006-2015 is shown by horizontal line at 0.63°C.

Annex 1.A.7: Recent trends in emissions and radiative forcing

Figure 1.2 shows a small increase in the estimated rate of human–induced warming since 2000, reaching 0.2°C per decade in the past few years. This is attributed (Haustein et al., 2017) to recent changes in a range of climate forcers, reviewed in this section.

Most studies partition anthropogenic climate forcers into two groups by their lifetime. CO_2 and other long–lived greenhouse gases such as nitrous oxide, sulphur hexafluoride and some halogenated gases contribute to forcing over decades and centuries. Other halogenated gases, ozone precursors and aerosols are defined as short–lived climate forcers (SLCF) due to their residence time of less than several years in the atmosphere. Although methane is either considered as a LLCF or SLCF in published studies or reports (Bowerman et al., 2013; Estrada et al., 2013; Heede, 2014; Jacobson, 2010; Kerr, 2013; Lamarque et al., 2011; Saunois et al., 2016a; WMO, 2015), we assign methane as a SLCF for the purpose of climate assessment, because its lifetime is comparable to or shorter than the thermal adjustment time of the climate system (Smith et al., 2012).

CO_2, methane and nitrous oxide are the most prominent contributors of anthropogenic radiative forcing, contributing 63%, 20% and 6% of the anthropogenic radiative forcing in 2016 respectively, as shown in Figure 14(a). Other long-lived greenhouse gases, including halogenated gases, and SLCFs such as tropospheric ozone are responsible of about 37% of the anthropogenic radiative

forcing (figures add up to more than 100% because of the compensating effect of aerosols). Emissions such as black carbon and sulphur dioxide form different types of aerosol particles, which interact with both shortwave and longwave radiation and alter clouds. The resulting net aerosol radiative forcing is spatially inhomogeneous and uncertain. Globally averaged, it is estimated to have reduced the globally averaged anthropogenic forcing by about 27% (figures from Myhre et al. (2013), updated: uncertainties in aerosol forcing in particular are reviewed in AR5, and will be reassessed in AR6. This report continues to work from the AR5 estimates.).

As shown in Figure 14 (b), the growth of CO_2 emissions has slowed since 2013 because of changes in the energy mix moving from coal to natural gas and increased renewable energy generation (Boden et al., 2015). This slowdown in CO_2 emission growth has occurred despite global GDP growth increasing to 3% y^{-1} in 2015, implying a structural shift away from carbon intensive activities (Jackson et al., 2015; Le Quéré et al., 2018). In 2016, however, anthropogenic CO_2 emissions are 36.18 $GtCO_2$ y^{-1} and have begun to grow again by 0.4% with respect to 2015 (Le Quéré et al., 2018). Global average concentration in 2016 has reached 402.3 ppm, which represents an increase of about 38.4% from 1850–1900 average (290.7 ppm).

Figure 14 (c) and (d) show that methane and nitrous oxide emissions, unlike CO_2, have followed the most emission–intensive pathways assessed in AR5 (Saunois et al., 2016b; Thompson et al., 2014). However, current trends in methane and nitrous oxide emissions are not driven in the same way by human activities. About 60% of methane emissions are attributed to human activities (e.g. ruminants, rice agriculture, fossil fuel exploitation, landfills and biomass burning, Saikawa et al., 2014; Saunois et al., 2016b), while about 40% of nitrous oxide emissions are caused by various industrial processes and agriculture (Bodirsky et al., 2012; Thompson et al., 2014). It is thus more complicated to link rates of emissions to economic trends or energy demands than is the case with CO_2 (Peters et al., 2011).

Estimates of anthropogenic emissions for methane and nitrous oxide are uncertain as shown by the difference between datasets in Figure 1.4 EDGARV4.2 (JRC, 2011) estimates and US–EPA projections give a global amount of methane emission ranging between 392.87 and 378.29 $TgCH_4 y^{-1}$ by 2016 which corresponds to a relative increase of 0.6–1% compared to 2015 emissions. However, livestock emissions in these databases are considered to be underestimated (Wolf et al., 2017). Similar uncertainties exist for anthropogenic N_2O emissions for which only US–EPA projections are available. According to US–EPA projections, anthropogenic N_2O emissions reach 11.2 TgN_2O y^{-1}, representing a relative increase of about 1% compared to 2016. Anthropogenic CH_4 and N_2O emissions also appear to respond to major economic crises.
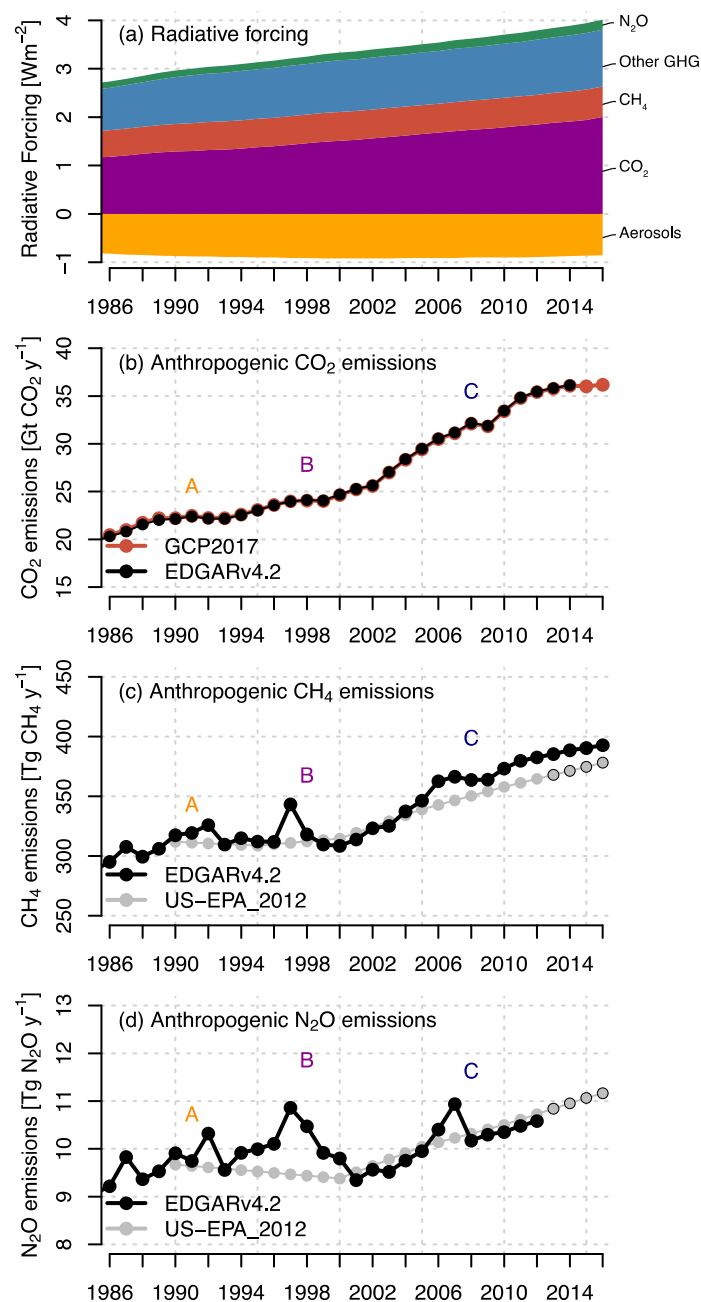
Technical Annex 1.A, Figure 14: Time series of anthropogenic radiative forcing (a), CO_2, methane (CH_4) and nitrous oxide (N_2O) emissions (b–d) for the period 1986–2016. Anthropogenic radiative forcing data is from Myhre et al., (2013), extended from 2011 until the end of 2017 with greenhouse gas data from Dlugokencky and Tans (2016), updated radiative forcing approximations for greenhouse gases (Etminan et al., 2016) and extended aerosol forcing following (Myhre et al., 2017). Bar graph shows the sum of different forcing agents. Anthropogenic CO_2 emissions are from the Global Carbon Project (GCP2017; Le Quéré et al., 2018), and EDGAR (Joint Research Centre, 2011) datasets. Anthropogenic emissions of CH_4 and N_2O (e) are estimated from EDGAR (JRC, 2011) and the US Environmental Protection Agency (EPA, 1990). Economic crisis (Former Soviet Union, A; Asian financial crisis, B; global financial crisis, C) are reported following the methodology of (Peters et al., 2011).

References

Bindoff, N. L., Stott, P. A., AchutaRao, K. M., Allen, M. R., Gillett, N., Gutzler, D., et al. (2013). "Detection and Attribution of Climate Change: from Global to Regional," in *Climate Change 2013: The Physical Science Basis. Contribution of Working Group I to the Fifth Assessment Report of the Intergovernmental Panel on Climate Change*, eds. T. F. Stocker, D. Qin, G.-K. Plattner, M. Tignor, S. K. Allen, J. Boschung, et al. (Cambridge, UK and New York, NY, USA: Cambridge University Press), 426–488.

Cowtan, K., Hausfather, Z., Hawkins, E., Jacobs, P., Mann, M. E., Miller, S. K., et al. (2015). Robust comparison of climate models with observations using blended land air and ocean sea surface temperatures. *Geophys. Res. Lett.* 42, 6526–6534. doi:10.1002/2015GL064888.

Cowtan, K., and Way, R. G. (2014). Coverage bias in the HadCRUT4 temperature series and its impact on recent temperature trends. *Q. J. R. Meteorol. Soc.* 140, 1935–1944. doi:10.1002/qj.2297.

Doxsey-Whitfield, E., MacManus, K., Adamo, S. B., Pistolesi, L., Squires, J., Borkovska, O., et al. (2015). Taking Advantage of the Improved Availability of Census Data: A First Look at the Gridded Population of the World, Version 4. *Pap. Appl. Geogr.* 1, 226–234. doi:10.1080/23754931.2015.1014272.

Etminan, M., Myhre, G., Highwood, E. J., and Shine, K. P. (2016). Radiative forcing of carbon dioxide, methane, and nitrous oxide: A significant revision of the methane radiative forcing. *Geophys. Res. Lett.* 43, 12,614-12,623. doi:10.1002/2016GL071930.

Foster, G., and Rahmstorf, S. (2011). Global temperature evolution 1979–2010. *Environ. Res. Lett.* 6, 044022. doi:10.1088/1748-9326/6/4/044022.

Fricko, O., Havlik, P., Rogelj, J., Klimont, Z., Gusti, M., Johnson, N., et al. (2017). The marker quantification of the Shared Socioeconomic Pathway 2: A middle-of-the-road scenario for the 21st century. *Glob. Environ. Chang.* 42, 251–267. doi:10.1016/j.gloenvcha.2016.06.004.

Geoffroy, O., Saint-Martin, D., Olivié, D. J. L., Voldoire, A., Bellon, G., and Tytéca, S. (2013). Transient climate response in a two-layer energy-balance model. Part I: Analytical solution and parameter calibration using CMIP5 AOGCM experiments. *J. Clim.* 26, 1841–1857. doi:10.1175/JCLI-D-12-00195.1.

Ghan, S. J., Smith, S. J., Wang, M., Zhang, K., Pringle, K., Carslaw, K., et al. (2013). A simple model of global aerosol indirect effects. *J. Geophys. Res. Atmos.* 118, 6688–6707. doi:10.1002/jgrd.50567.

Gregory, J. M., Andrews, T., Good, P., Mauritsen, T., and Forster, P. M. (2016). Small global-mean cooling due to volcanic radiative forcing. *Clim. Dyn.* 47, 3979–3991. doi:10.1007/s00382-016-3055-1.

Hartmann, D. J., Klein Tank, A. M. G., Rusticucci, M., Alexander, L. V, Brönnimann, S., Charabi, Y. A.-R., et al. (2013). "Observations: Atmosphere and Surface," in *Climate Change 2013: The Physical Science Basis. Contribution of Working Group I to the Fifth Assessment Report of the Intergovernmental Panel on Climate Change*, eds. T. F. Stocker, D. Qin, G.-K. Plattner, M. Tignor, S. K. Allen, J. Boschung, et al. (Cambridge, UK and New York, NY, USA: Cambridge University Press), 159–254. doi:10.1017/CBO9781107415324.008.

Haustein, K., Allen, M. R., Forster, P. M., Otto, F. E. L., Mitchell, D. M., Matthews, H. D., et al. (2017). A real-time Global Warming Index. *Sci. Rep.* 7, 15417. doi:10.1038/s41598-017-14828-5.

Kirtman, B., Adedoyin, A., and Bindoff, N. (2013). "Near-term Climate Change: Projections and Predictability," in *Climate Change 2013: The Physical Science Basis. Contribution of Working Group I to the Fifth Assessment Report of the Intergovernmental Panel on Climate Change*, eds. T. F. Stocker, D. Qin, G.-K. Plattner, M. Tignor, S. K. Allen, J. Boschung, et al. (Cambridge, UK and New York, NY, USA: Cambridge University Press), 953–1028. doi:10.1017/CBO9781107415324.023.

Kopp, R. E., Kemp, A. C., Bittermann, K., Horton, B. P., Donnelly, J. P., Gehrels, W. R., et al. (2016). Temperature-driven global sea-level variability in the Common Era. *Proc. Natl. Acad. Sci.* 113, 1–8. doi:10.1073/pnas.1517056113.

Marcott, S. A., Shakun, J. D., Clark, P. U., and Mix, A. C. (2013). A reconstruction of regional and global temperature for the past 11,300 years. *Science (80-.).* 339, 1198–201. doi:10.1126/science.1228026.

Matthes, K., Funke, B., Andersson, M. E., Barnard, L., Beer, J., Charbonneau, P., et al. (2017). Solar forcing for CMIP6 (v3.2). *Geosci. Model Dev.* 10, 2247–2302. doi:10.5194/gmd-10-2247-2017.

Meinshausen, M., Smith, S. J., Calvin, K., Daniel, J. S., Kainuma, M. L. T., Lamarque, J., et al. (2011). The RCP greenhouse gas concentrations and their extensions from 1765 to 2300. *Clim. Change* 109, 213–241. doi:10.1007/s10584-011-0156-z.

Millar, R. J., Nicholls, Z. R., Friedlingstein, P., and Allen, M. R. (2017). A modified impulse-response representation of the global near-surface air temperature and atmospheric concentration response to carbon dioxide emissions. *Atmos. Chem. Phys.* 17, 7213–7228. doi:10.5194/acp-17-7213-2017.

Myhre, G., Highwood, E. J., Shine, K. P., and Stordal, F. (1998). New estimates of radiative forcing due to well mixed greenhouse gases. *Geophys. Res. Lett.* 25, 2715–2718. doi:10.1029/98GL01908.

Myhre, G., Samset, B. H., Schulz, M., Balkanski, Y., Bauer, S., Berntsen, T. K., et al. (2013a). Radiative forcing of the direct aerosol effect from AeroCom Phase II simulations. *Atmos. Chem. Phys.* 13, 1853–1877. doi:10.5194/acp-13-1853-2013.

Myhre, G., Shindell, D., Bréon, F., Collins, W., Fuglestvedt, J., Huang, J., et al. (2013b). "Anthropogenic and natural radiative forcing," in *Climate Change 2013: The Physical Science Basis. Contribution of Working Group I to the Fifth Assessment Report of the Intergovernmental Panel on Climate Change*, eds. T. F. Stocker, D. Qin, G.-K. Plattner, M. Tignor, S. K. Allen, J. Boschung, et al. (Cambridge, UK and New York, NY, USA: Cambridge University Press), 658–740. doi:0.1017/CBO9781107415324.018.

Prather, M., Flato, G., Friedlingstein, P., Jones, C., Lamarque, J.-F., Liao, H., et al. (2013). "Annex II: Climate System Scenario Tables," in *Climate Change 2013: The Physical Science Basis. Contribution of Working Group I to the Fifth Assessment Report of the Intergovernmental Panel on Climate Change* (Cambridge, MA, USA and London, England: Cambridge Univeristy Press).

Richardson, M., Cowtan, K., and Millar, R. J. (2018). Global temperature definition affects achievement of long-term climate goals. *Environ. Res. Lett.* 13, 054004.

Sachs, J., Schmidt-Traub, G., Kroll, C., Durand-Delacre, D., and Teksoz, K. (2017). An SDG Index and Dashboards - Global Report. New York, NY, USA.

Smith, C. J., Forster, P. M., Allen, M., Leach, N., Millar, R. J., Passerello, G. A., et al. (2018). FAIR v1.3: A simple emissions-based impulse response and carbon cycle model. *Geosci. Model Dev.* doi:10.5194/gmd-2017-266.

Stevenson, D. S., Young, P. J., Naik, V., Lamarque, J. F., Shindell, D. T., Voulgarakis, A., et al. (2013). Tropospheric ozone changes, radiative forcing and attribution to emissions in the Atmospheric Chemistry and Climate Model Intercomparison Project (ACCMIP). *Atmos. Chem. Phys.* 13, 3063–3085. doi:10.5194/acp-13-3063-2013.

Toohey, M., Stevens, B., Schmidt, H., and Timmreck, C. (2016). Easy Volcanic Aerosol (EVA v1.0): an idealized forcing generator for climate simulations. *Geosci. Model Dev.* 9, 4049–4070. doi:10.5194/gmd-9-4049-2016.